An inverse-scattering sub-series for predicting the correct spatial location of reflectors: Initial analysis, testing and evaluation

Simon A. Shaw (BP, shawsa@bp.com)

Abstract

The inverse scattering series inverts for medium properties from only the measured wavefield and information about a chosen reference medium. Motivated by the need to successfully image targets beneath complex overburdens, there is new research into the potential of this series to perform the specific inversion task of seismic depth migration without requiring a priori information about the Earth's properties. A sub-series of the inverse scattering series has been identified that is responsible for locating seismic events in depth with reflection data. To evaluate the efficacy of this sub-series for imaging, it is systematically exposed to varying degrees of realism, under controlled conditions. This paper summarizes an initial analysis of the behavior of the imaging algorithm in 1-D when the contrast between actual and reference media is varied, and when truncating frequency and time apertures. As predicted analytically, it is found that the performance improves when the contrast is reduced and when the maximum frequency is lower. Finally, it is demonstrated that the algorithm remains effective even when missing zero frequency.

Introduction

Seismic imaging through complex media (e.g., salt, basalt and karsted sediments) is one of the most difficult problems facing exploration seismologists. This is because the accuracy of current methods for imaging seismic data is heavily dependent on the degree to which we can estimate Earth properties above the target. For example, with traditional migration algorithms, to focus an image at the correct depth, the algorithm must be supplied with the precise velocity. Consequently, a great deal of research has been conducted into methods that improve our ability to estimate seismic velocities. An alternative approach is to research new methods of imaging and inversion that are more flexible in their assumptions about the degree to which we already know the Earth's properties. In this paper, we discuss one of these new candidate methods, and present some early results of tests that assess the method's robustness under realistic data conditions.

Following the successful development of inverse scattering algorithms to remove free-surface and internal multiples (Weglein et al. 1997), new research is aimed at examining the potential of this series to migrate seismic reflection data to the correct depth without knowing the velocity (Weglein et al., 2000). By separating inversion tasks, terms in the inverse scattering series have been identified that are responsible for locating reflectors in their correct spatial location (Weglein et al., 2001a). Collectively, these terms constitute an inverse-scattering sub-series for imaging. Assumptions of this algorithm are that the source wavelet is known, and that multiple reflections have been removed from the data. It can be generalized to 3-D, and with wave equations for Earth models of increasing complexity.

1-D Inverse Scattering Sub-Series for Imaging

For a wave traveling in a 1-D constant density acoustic medium, the pressure $P(z,\omega)$ is governed by

$$\left[\frac{d^2}{dz^2}+\frac{\omega^2}{c_0^{\,2}}\left(1-\alpha(z)\right)\right]P(z,\omega)=0 \qquad (1)$$

where ω is the angular frequency, c_0 is the homogenous reference velocity, $V = k^2\alpha$ and $k = \omega/c_o$. In this context, the inverse problem is to determine α where

$$\alpha=\alpha_1+\alpha_2+\ldots \qquad (2).$$

The inverse series can be solved for α_1, α_2,… and for the 1-D normal incidence case, a subset of terms, α_{migr}, that focuses the input reflection data at the correct depth have been identified (Weglein et al., 2001b) as

$$\alpha_{migr}=\alpha_1(z)-\frac{1}{2}\left[\frac{d}{dz}\alpha_1(z)\int_0^z\alpha_1(z')dz'+\frac{d}{dz}\alpha_1(z)\int_0^z\alpha_2(z')dz'+\frac{d}{dz}\alpha_2(z)\int_0^z\alpha_1(z')dz'+\cdots\right] \qquad (3).$$

In this particular case, α_1 consists of step functions with interfaces at depths that c_0 would predict from the data's travel times. When the actual velocity $c(z)$ above a reflector is not equal to c_0, then α_1 will predict the incorrect depth. Successive terms in the imaging sub-series can be visualized in 1-D as a series for a corrective box-like function that, in effect, removes the interfaces at the incorrect depth and creates the interfaces at the correct depth.

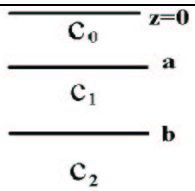

Figure 1: Model of a single layer with velocity c_1.

Consider the simple case illustrated in Fig. 1, for a single layer with velocity c_1. We assume that multiples have been removed and the wavelet is zero phase with unit amplitude. We choose the reference velocity to be c_0. Then, for an incident plane wave, α_1 will be the difference of two step functions, i.e., a box starting at a and ending at the pseudo depth b', as illustrated in Fig. 2. The task of imaging at the correct depth can be interpreted as the portions of $\alpha_2 + \alpha_3 + \ldots$ that construct the dashed box starting at b' and ending at b.

Convergence and Rate of Convergence

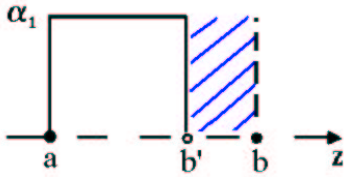

Figure 2: Interpreting the task of moving the reflector from pseudo depth b' to actual depth b for the case where $c_1 > c_0$ and $c_1 > c_2$.

Consider the misplaced reflector in Fig. 2, where α_1 is a box from a to b' that needs to become a box from a to b. The box that moves b' to the correct depth b (illustrated by the shaded region) is Fourier transformed and then the expression $e^{ik(b'-b)}$ is expanded in its always-convergent Taylor Series

$$e^{ik(b'-b)} = \sum_{n=0}^{\infty} \frac{[ik(b'-b)]^n}{n!}.$$

Then, to within a scalar multiplier, the shaded region can be written (Weglein et al. 2001b)

$$\mathrm{H}(z-b') - \mathrm{H}(z-b) = \int \frac{e^{ik(z-b')}}{ik} \sum_{n=1}^{\infty} \frac{[ik(b'-b)]^n}{n!} dk \quad (4).$$

Hence the move from the incorrect depth b' to the actual depth b consists of a sum of delta functions and derivatives of delta functions centered at b' and weighted by functions of the distance $(b'-b)$. This series converges for any finite $k(b'-b)$. Furthermore, for this 1-D, constant density, acoustic model, proximity of b to b' and absence of very high frequencies will aid the rate of convergence.

Approach to Analysis and Testing

Once an algorithm has been derived and comprehended analytically, the next step is to investigate whether it will be robust and effective in a practical setting. We begin our numerical analysis by testing the algorithm with ideal input data, and by varying the Earth model parameters. The Earth model is a variable over which we have no control in the real world and therefore constitutes the critical first test. If the algorithm is not effective (by some reasonable measure, e.g., series convergence) having idealized the conditions that we are able to influence, then further testing is unwarranted, and we must seek a new algorithm.

On the other hand, if the algorithm is found to be effective for a practical suite of Earth parameters, then we can investigate its performance with imperfect input data. Data are imperfect when they are aperture-limited (e.g., frequency band-limited) or when an assumption in the method is violated (e.g., added noise, residual multiple, or an unknown wavelet). It is expected that there will be some loss in effectiveness when the method assumptions are violated, but an understanding of the algorithm's sensitivity under these conditions is essential to developing a practical algorithm for field data.

In this paper, we consider the 1-D manifestation of the algorithm, and so we have only a single degree of freedom in our data. The sensitivities of the imaging sub-series to frequency bandwidth, time aperture, and contrast (between actual and reference media) are analyzed numerically.

1-D Numerical Analysis

To analyze the response of the imaging sub-series (Eq. 3) to different input data attributes, we have performed a suite of numerical tests for the model illustrated in Fig. 1. A summary of these tests is presented here.

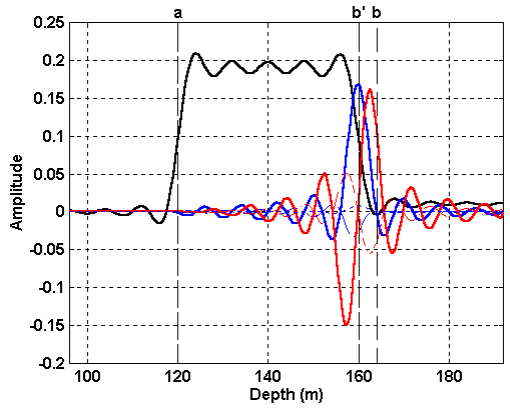

Figure 3: Band-limited (0–125Hz) imaging sub-series components from the first three terms of the inverse series (α_{1-3}). Model parameters are c_0=2000m/s, c_1=2200m/s, c_2=2010m/s, a=120 m, b=164 m.

Figure 3 shows the individual components of α_{migr}, from the first three terms of the inverse series, for a chosen set of model parameters described in the caption. The black box is α_1, and the components from α_2 and α_3 are colored red and blue. The sample rate is higher than the maximum frequency in the data, so the data are not aliased. The trace length is 640 ms, which is long enough to mitigate a truncation of the time aperture. Studying Fig. 3, besides the α_1 box, the two highest amplitude components are a band-limited delta function (a sinc function) and a derivative of a sinc function, both centered at b'. When summed, these two terms act to extend the misplaced interface in α_1 from b' towards b. This is demonstrated in Fig. 4 where panel (ii) shows the sum of the imaging terms, α_{migr}, and panel (iii) shows the derivative of this result where the reflector at b' has moved approximately 87% of the distance to b using, what is essentially, two terms beyond conventional imaging. With all other model and data parameters remaining constant, if we truncate the time aperture from 640 ms to 320 ms, and recalculate α_{migr}, with the same number of terms then the move from b' to b loses some effectiveness, but still manages 75% of the total distance.

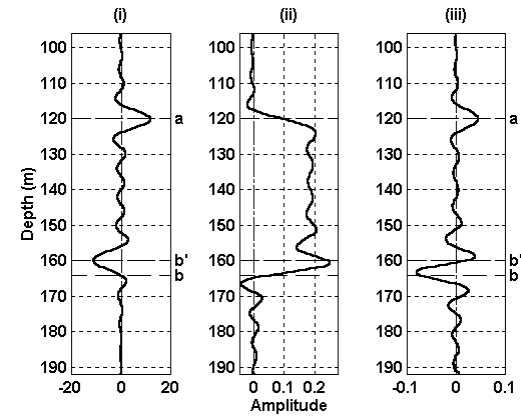

Figure 4: Imaging sub-series for 0–125Hz band-limited input data. The model is described in Fig. 3. (i) d/dz[$\alpha_1(z)$] equivalent to migration with the reference velocity. The second reflector is misplaced at b'. (ii) Sum of the imaging sub-series using three terms in the inverse scattering series. (iii) Depth derivative of result in (ii) shows the location of the lower reflector has moved from b' towards b.

Figure 5 (i-iv) shows the component imaging terms for a suite of four different permutations of c_0, c_1 and c_2. Panel (i) is the same example as in Fig. 3. For each possible Earth model, when the terms are summed, the deeper reflector moves from incorrect depth, b', to correct depth, b.

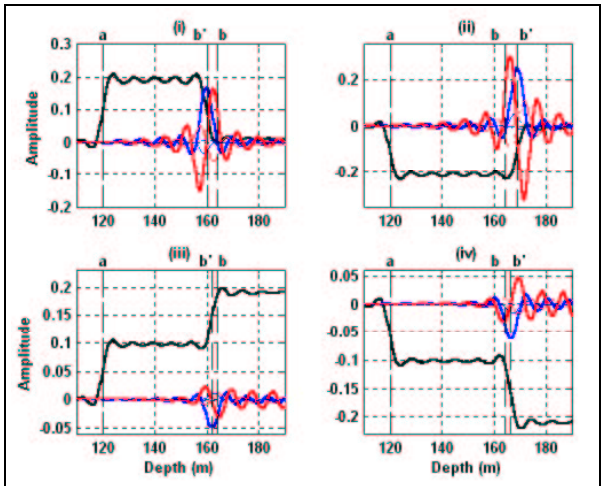

Figure 5: A suite of different Earth model parameters c_1 and c_2. Input data are band-limited (0–125Hz) and imaging sub-series components from the first three terms of the inverse series (α_{1-3}) are displayed. Parameters are c_0=2000m/s, a=120 m, b=164 m and (i) c_1=2200m/s, c_2=2010m/s; (ii) c_1=1800m/s, c_2=1990m/s; (iii) c_1=2100m/s, c_2=2200m/s; (iv) c_1=1900m/s, c_2=1800m/s.

Results for 0–70 Hz band-limited input data have been studied. As predicted analytically, the convergence properties of the imaging sub-series improve for lower maximum frequency. In this case, the move from b' to b is achieved with the three terms.

The effect of increasing the contrast between the actual medium and the reference medium has been examined. When the contrast is increased to 15% (from 10% in Fig. 4) then the deeper reflector moves 63% of the distance from b' to b as opposed to 87%,

using three terms in both cases. If this contrast is reduced from 10% to 5% then we find that, using three terms, the reflector at b' is relocated to a depth even closer to b, about 8% of $(b' - b)$ beyond b.

We have removed the zero frequency component of the input data, and recalculated the same sub-series terms as before. When these terms are summed, we get the results displayed in Fig. 7(iii) that shows the misplaced reflector at b' moves approximately 85% of the distance to b. If the same data are also truncated in time from 640 ms to 320 ms then we get the result shown in Fig. 8, where the move is approximately 50% of $(b' - b)$. This time, the reflector at a has moved shallower.

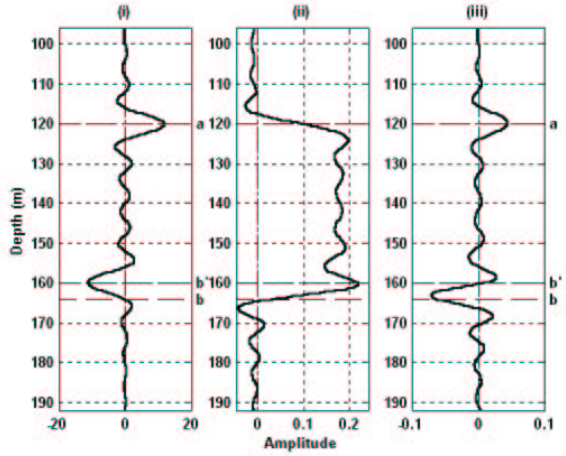

Figure 7: Missing zero frequency: band-limited (1–125Hz) imaging sub-series for the model described in Figure 3. Panels (i–iii) are described in Fig. 4.

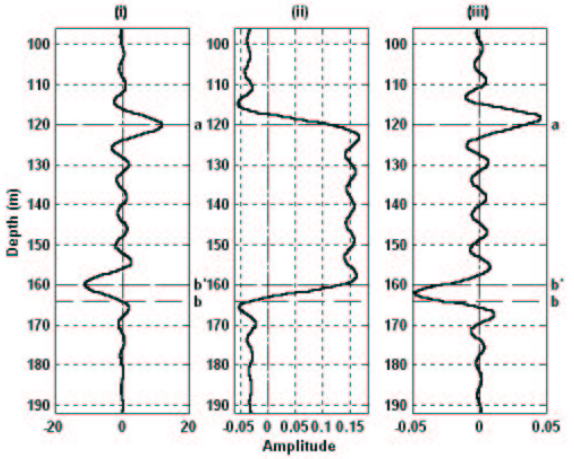

Figure 8: Truncated input data in time and missing zero frequency: band-limited (1–125Hz) imaging sub-series for the model described in Figure 3. Panels (i–iii) are described in Fig. 4.

Conclusions and Future Work

Under a controlled suite of numerical tests summarized here, we have found the convergence of the inverse scattering sub-series for imaging in 1-D is effective for all the tested Earth model parameters with idealized input data. As anticipated, optimal results are achieved when our input data contain low frequencies, when the maximum frequency is lower, and when the contrast between the reference medium and actual medium is reduced. It remains effective even when missing zero frequency.

We plan to investigate recasting the algorithm with a view to better separating the tasks of imaging and inversion. As presented, the imaging series starts with a box-like function, α_1, whose amplitude is related to an inversion for the medium parameters – a different task. If we can re-express the algorithm in terms of a spike-like function, there is a precedent for being able to further improve the robustness of an algorithm that performs just a single task on our recorded data.

References

Weglein, A.B., Gasparotto, F.A., Carvalho, P.M., and Stolt, R.H. (1997) "An inverse scattering series method for attenuating multiples in seismic reflection data": Geophysics, 62, pp. 1975–1989.

Weglein, A.B., Matson, K.H., Foster, D.J., Carvalho, P.M., Corrigan, D., Shaw, S.A. (2000) "Imaging and inversion at depth without a velocity model" 70th Annual Meeting, SEG, Calgary, Canada.

Weglein, A.B., Foster, D.J., Matson, K.H., Shaw, S.A., Carvalho, P.M., Corrigan, D (2001a) "An inverse scattering sub-series for predicting the spatial location of reflectors without the precise reference medium and wave velocity " submitted to 71st Annual Meeting, SEG, San Antonio, Texas.

Weglein, A.B., Foster, D.J., Matson, K.H., Shaw, S.A., Carvalho, P.M., Corrigan, D (2001b) "An inverse scattering sub-series for predicting the spatial location of reflectors without knowing or determining the propagating medium" submitted to 7th International Congress, SBGf, Salvador, Brazil.

Acknowledgments

Art Weglein is thanked for technical contributions and support. Ken Matson is also thanked for useful discussions. Doug Foster, Paulo Carvalho, Dennis Corrigan, Craig Cooper and BP Management are gratefully acknowledged.

AVO analysis based on purely kinematic imaging

Dominique Rousset, Univ. of Pau, France, Hervé Perroud, Univ. of Pau, France, Martin Tygel, Univ. of Campinas, Brazil

Summary

If we assume that the kinematic imaging problem is solved, we get valuable macrovelocity model and depth description of the interfaces. By means of ray tracing, these results can be used to extract reflected signal coming from a common reflection point (CRP), ensuring that the interface characteristics don't vary from trace to trace for the selected event. Velocity field, interface location dip and curvature and medium characteristics can be used to derive a geometrical spreading correction factor that will be used to compensate the recorded signal, giving the true amplitude reflected signal.

We use a synthetic data set computed with finite differences. The reference model is a simple reservoir like structure, in an off-shore context, which is perturbated, for compressional and shear velocities in the sub reflector medium in order to keep travel times unaltered while substantially modifying the amplitude of the reflected signal.

In this paper, we compare this approach to conventional AVO analysis of seismic data.

Introduction

Beyond imaging, analysis and interpretation of the amplitude of the reflected signal is a key point of complete interpretation of seismic signal, especially in reservoirs. Instead of trying to perform preserved amplitude processing, which is time consuming and quite difficult, one can use purely kinematic processing which allows for a quite good geometrical description of the interfaces. One extra result of this process is a macro velocity field.

Once reflector geometry and velocity field are known, dynamic ray tracing is an efficient tool to estimate geometrical spreading (Rousset et al., submitted). Raw amplitude, corrected for geometrical spreading is a good estimate of the true amplitude variation with offset. In case where the amplitudes are measured in a common reflection point gather (CRP) this gives an accurate measure of the local reflectivity of the interface. Additional amplitude parameters, such as amplitude transmission losses on the main interfaces can also be taken into account.

We analyze amplitude versus offset and amplitude versus angle, since ray tracing allow us to know the incidence angles on the target reflector.

Our analysis consists in the three following steps:

1. Synthetic data are computed with 2-D *P-Sv* finite differences, allowing for 2-D accurate computation of AVO/AVA and cylindrical divergence. This kind of modelling has a built-in ability to take into account change of reflectivity with model parameters and the angle of incidence.
2. We can then use the the velocity field to compute the arrival times and geometrical spreading correctionb factor for a CRP, ensuring that the illuminated surface is as small as possible.
   - Since the true velocity field is known, we can use it to get an exact solution.
   - We also investigate the consequences of a less perfectly known velocity model, like it would be in "real" processing.
3. Geometrical spreading correction factor is applied to the extracted AVO curves. AVO curves are discussed and compared to conventional AVO analysis.

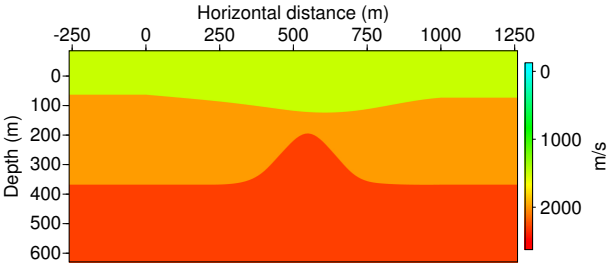

Fig. 1: Dome-like compressional velocity model

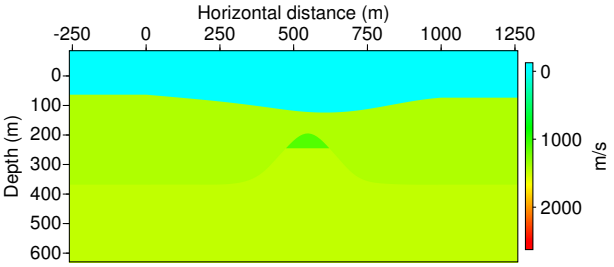

Fig. 2: Dome-like shear velocity model

Synthetic data computation

Computations have been carried on using the velocity/stress formulation on a staggered grid (see Tab. 1 for parameters), allowing for P and S_v waves to appear and interact (Virieux, 1986). This numerical scheme is

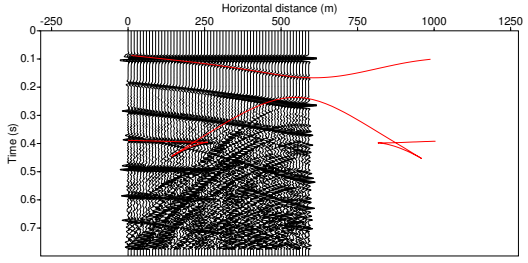

Fig. 3: Synthetic zero offset section. Redlines indicate primary reflections on the water bottom and the top of the dome

appropriate for taking into account water/solid transition. Small vertical grid space (and consequently high computation time) is required to minimize scattering on the discrete edges of the water bottom.

Close to the free surface, pressure tends to be null and particle velocity comes to vertical, making comparison with ray tracing amplitudes difficult. Sources and receivers are thus placed 85 meters under the upper free surface. One drawback of this particular acquisition design is the appearance of strong and long period ghosts and multiples. Long offset ringing data have therefore been muted in subsequent processing.

Number of shots	65
Shot spacing	10 m
Type of receivers	Pressure
Number of receivers	201
Hydrophone spacing	5 m
Final time sampling	1 ms
X grid size	0.8 m
Z grid size	0.2 m
Time step	0.044 ms

Table 1: Synthetic data computation parameters

Figure 3 presents the zero offset section of the illuminated part of the model. Note the triplication caused by the inner part of the dome and the good fit with ray-traced arrival times.

Kinematic processing

Two different processing are applied, one uses the exact velocity field used to compute the synthetics. The other one is derived from a sandard imaging process.

As an example, one can see the result of prestack Kirchhoff depth migration without weights applied to the reference data, equalized with AGC.

Conventional tools for velocity analysis migration velocity analysis etc are used to derive a velocity model. T

Dynamic ray tracing

Using the real velocity field, selected Common Reflection Points gathers can be computed. Using CRP gathers ensures that medium properties and geometrical characteristics (dip and curvature) do not vary for the reflection event and allows a direct comparison with the depth migrated images. One drawback of this choice is that CRP gather is event dependent and another is that it relies on the velocity model.

CRP gathers are computed by first choosing the CRP and second looking for the rays corresponding to a regular sampling in offset. Amplitudes are linearly interpolated in the source/geophone space to match CRP gather traces locations. Finite differences events amplitudes are picked as the maximum of the analytic traces, avoiding phase variations and small picking errors, in a time window centered on the predicted travel time.

Dynamic ray tracing allows to know the arrival time of the reflected event. It also allows to estimate the three factors which influence the predicted amplitude:

1. Geometrical spreading (cylindrical for line source and receivers)
2. Focusing and defocusing due to reflector curvature using the optical conjugate equation (de Bazelaire and Derain, 1988)
3. Model reflectivity, computed using V_P, V_S, ρ and incidence angle (Aki and Richards, 1980).

AVO analysis

Results from 2 selected CRP's are shown below (fig. 5 and 6). For each one, the following diagrams are given:

1. On the left, the CRP gather, extracted from raw data, without any amplitude correction. The traces are positive, since we have represented the analytic amplitude, removing the waveform. In red is the picking window derived from the ray-tracing.
2. The ray pattern illustrates the CRP position as well as the ray-paths. Longer ray paths can explain lower amplitudes, even with a higher reflectivity.
3. Lower left figure shows the picked amplitude in the synthetic data (crosses) along with the computed amplitude with ray-tracing. Since the seismic source in the finite difference computation is not calibrated, all the amplitudes have been normalized with respect to the first ray amplitude of CRP 162.
4. Upper right figure shows the geometrical spreading computed with ray-tracing.

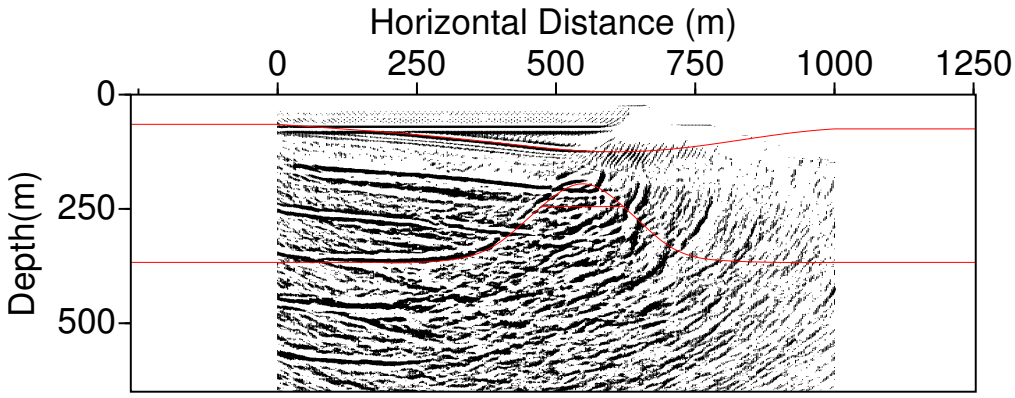

Fig. 4: kinematic processing

5. Lower right figure shows the true reflected amplitude from the selected event. It is obtained by correcting the raw amplitude with the geometrical spreading factor. This correction corrects the reflectivity for the apparent ray length but not for the loss of energy due to the differences in transmission coefficients during the trip of the various rays in the CRP.

Conclusions

To conclude this study, we can say that :

- this procedure enhances AVO anomalies due to lithological changes only and helps to discriminate between other origin for the change in amplitude;
- unlike preserved amplitude prestack migration, it can be used on selected targets only, saving computation time;
- it is conceptually easy to extend these results to 3-D data sets, using an adequate ray tracing code.

Acknowledgements

This work began while Martin Tygel was a visiting professor in University of Pau. Unité Mixte de Recherches 5831 is sponsored by the ministère de l'Éducation Nationale, Centre National de la Recherche Scientifique and TotalFinaElf. All seismic processing presented in this paper has been carried on using the Seismic Unix Package from Colorado School of Mines. All the graphics editing has been performed using LaTex, xfig and other free software.

References

Aki, K., and Richards, P. G., 1980, Quantitative seismology: Theory and methods: W. H. Freeman and Co.

de Bazelaire, E., and Derain, J. F., 1988, Modeling by optical imagery: 58th Annual Internat. Mtg., Soc. Expl. Geophys., Expanded Abstracts, Session:S19.8.

Rousset, D., Tygel, M., and Perroud, H., submitted, Attaching true amplitude to kinematically migrated images: submitted to J. Seismic Explor.,.

Virieux, J., 1986, P-SV wave propagation in heterogeneous media - Velocity-stress finite-difference method: Geophysics, **51**, no. 04, 889–901.

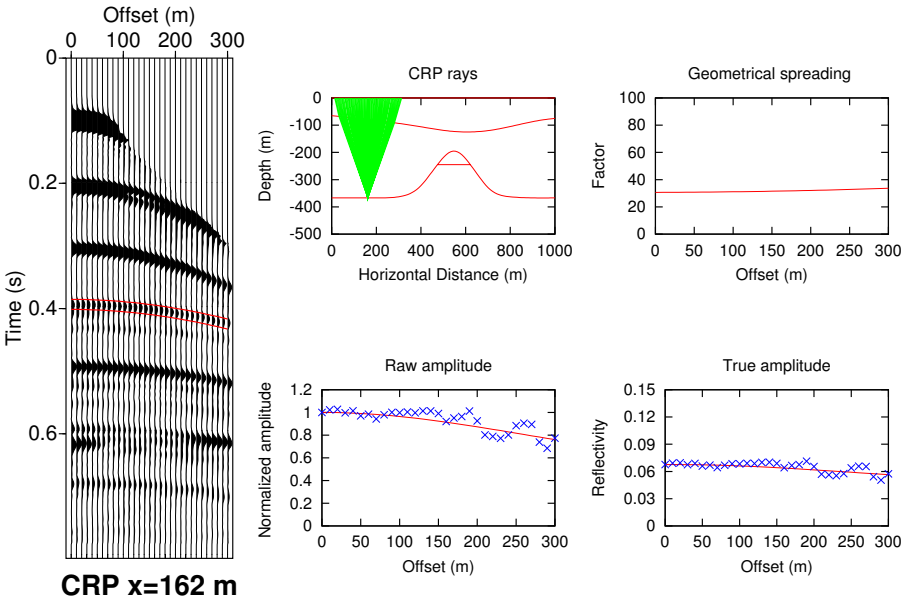

Fig. 5: Reference CRP, outside the V_S anomaly zone. Note the very good fit between predicted and picked true amplitudes

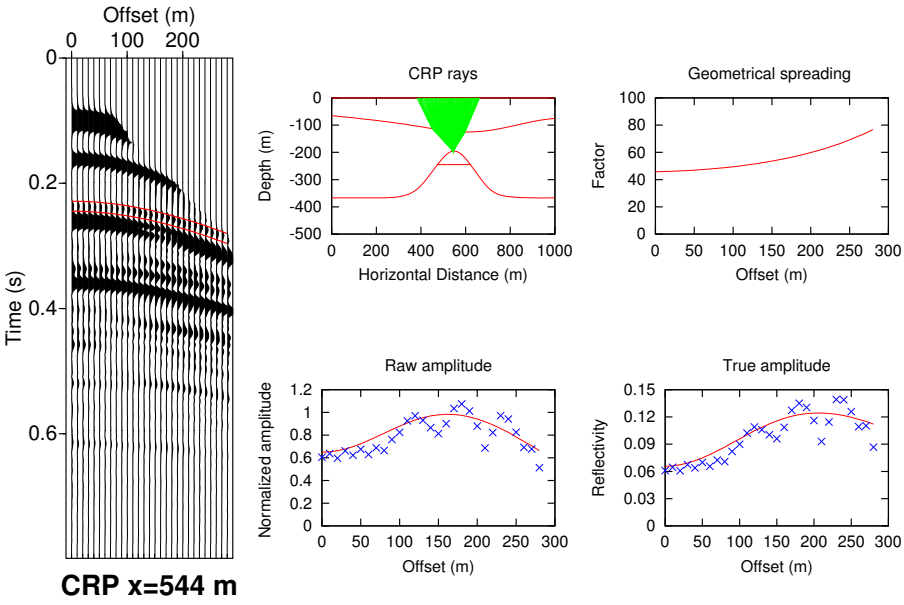

Fig. 6: CRP from the top of the dome, within the anomaly area. True amplitudes are stronger and very sensitive to the incidence angle

Common-Reflection-Surface Stack and attributes

Steffen Bergler†, Yonghai Zhang†, Pedro Chira†, Kai-Uwe Vieth†, and Peter Hubral†

Abstract

The Common-Reflection-Surface Stack which has been established over the past years as an alternative to standard data-driven imaging techniques not only yields high-quality stack sections from multi-coverage reflection pre-stack data but also provides—as by-product to the stacked section—important wavefield attributes. With the knowledge of the near-surface velocity only these attributes can be extracted from the stacking parameters which constitute the Common-Reflection-Surface stacking operator. The wavefield attributes are of use for a multitude of seismic applications. These include among others the computation of the geometrical spreading factor, the determination of the projected Fresnel zone, or the inversion of the macro-velocity model.

Introduction

Primarily, the Common-Reflection-Surface (CRS) Stack has been introduced to simulate zero-offset (ZO) sections from 2-D seismic reflection pre-stack data (Müller et al., 1998), where sources and receivers are supposed to be located on a straight measurement line (the seismic line). To avoid confusions, we want to refer to this case in the following as the ZO CRS Stack. The ZO CRS operator is derived by means of paraxial ray theory and has a three-parameter description. If the near-surface velocity in the vicinity of a coincident source/receiver location is known the three stacking parameters determined by means of a coherency analysis directly from the data (Jäger et al., 2001) can be related to important wavefield attributes. These attributes are the wavefront curvatures of two hypothetical waves at the coincident source/receiver location and their identical propagation direction (emergence angle) at this point. In this way the stacking parameters obtain a "physical" meaning: as the description of the ZO CRS stacking operator is based on the assumption of curved reflector segments in the subsurface, one can deduce information about the reflectors' positions, dips, and curvatures from the wavefield attributes. In case of varying elevations along the seismic line, the parameterization of the ZO CRS stacking operator has to be modified to obtain wavefield attributes with a well-defined geometrical meaning. In the first part of this contribution, we therefore introduce the modified ZO CRS stacking operator where the parameters give attention to the influence of the curved measurement line.

Moreover, the three-parameter ZO CRS stacking operator has been recently extended to simulate any specified 2-D finite-offset (FO) section (e.g., a common-offset (CO) section), where now five stacking parameters constitute the FO CRS stacking operator (Zhang et al., 2001). With the FO CRS stacking operator the reflection event for an arbitrary offset can be approximated. Therefore, also large-offset reflections can be utilized in the FO CRS stacking process. Zhang et al. (2001) related the five parameters to wavefield attributes, thus, giving the parameters a geometrical meaning. These attributes are two angles and three wavefront curvatures, which can enter, for instance, into the calculations of the geometrical spreading factor or can be used in techniques like Stereotomography (Billette and Lambaré, 1998). In the second part of this contribution, we outline the FO CRS method and its application.

Zero-offset CRS Stack for a curved measurement line

For the ZO case, the three stacking parameters of the CRS stacking operator for 2-D media can be related to wavefield attributes if the near-surface velocity in the vicinity of the coincident source/receiver (in the following denoted by SG) location is available. Theses attributes are associated with the two so-called hypothetical eigenwaves which are the normal-incidence-point (NIP) wave and normal (N) wave (Hubral, 1983) propagating along the ZO (normal) ray. The wavefield attributes are given by the emergence angle β of the eigenwaves and the wavefront curvatures K_{NIP} and K_N, respectively, determined at SG. If sources and receivers are located on a curved measurement line, the influence of the topography on the data-determined attributes have to be taken into account to properly evaluate β, K_{NIP}, and K_N. If we denote the uncorrected values of the three wavefield attributes derived from the data ,

†Geophysical Institute, University of Karlsruhe, Germany

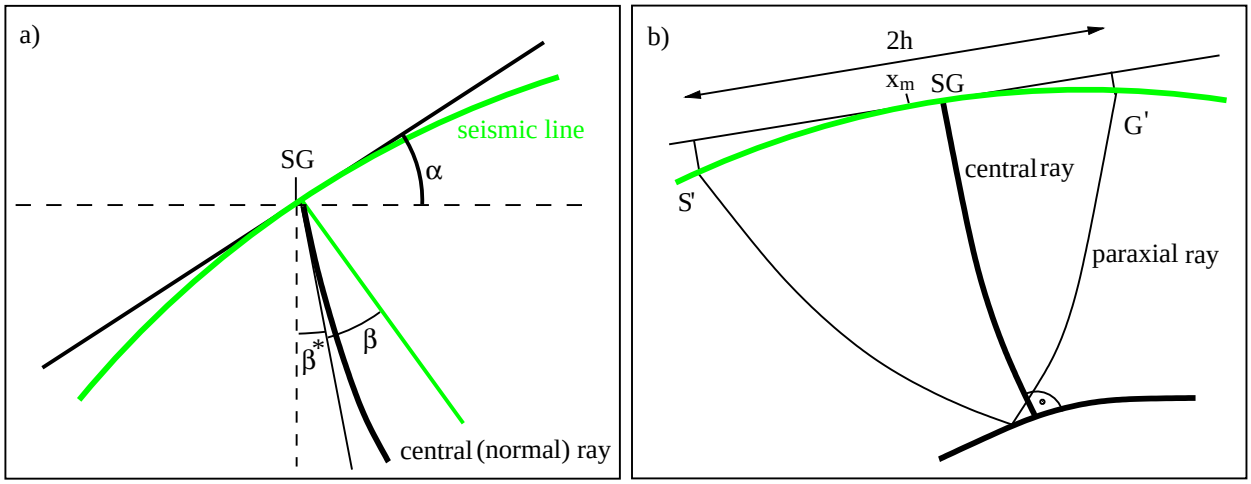

Figure 1: a): The seismic line has in the vicinity of SG the curvature K_S which is indicated by the circular arc (depicted in light gray). α is the local dip of the seismic line, β is the angle between the central ray and the normal to the seismic line at SG, and β^* is the angle between the central ray and the vertical line through SG. b): Definition of source and receiver coordinates of a paraxial ray for a curved measurement line with respect to SG.

i.e. the values based on the assumption of a straight measurement line, by β^*, K^*_{NIP}, and K^*_N then the correct values β, K_{NIP}, and K_N are given by the following relations:

$$\beta^* = \beta - \alpha \tag{1}$$

$$K^*_{NIP}\,\cos^2\beta^* = K_{NIP}\cos^2\beta - K_S\cos\beta \tag{2}$$

$$K^*_{N}\,\cos^2\beta^* = K_{N}\cos^2\beta - K_S\cos\beta\,, \tag{3}$$

where α denotes the dip and K_S the local curvature of the seismic line at SG (see Figure 1a). Both parameters are assumed to be known. Please note, K_S is positive if the curved measurement line falls below its tangent at the SG. Substituting these relations into the ZO CRS stacking operator (as given, e.g., by Mann et al., 1999) yields

$$\begin{aligned} t^2 = &\left(t_0 + 2\,\frac{\sin\beta}{v}\,x_m\right)^2 \\ &+ \frac{2}{t_0}\left(K_N\cos^2\beta - K_S\cos\beta\right)x_m^2 \\ &+ \frac{2}{t_0}\left(K_{NIP}\cos^2\beta - K_S\cos\beta\right)h^2\,, \end{aligned} \tag{4}$$

where t_0 is the traveltime along the central ray and v denotes the near-surfave velocity at SG. The offset $2\,h$ and midpoint x_m refer to the projections of all shot-receiver pairs in direction of the surface normal at SG onto the tangent at this point (see Figure 1b). Comparing the coeffients of the traveltime formula (4) with the hyperbolic traveltime

$$\begin{aligned} t^2 = &\left(t_0 - 2\,\frac{\sin\beta}{v}\,x_m\right)^2 \\ &+ 2\,t_0\left[\left(\frac{A-1}{B}\right)x_m^2 + \left(\frac{A+1}{B}\right)h^2\right] \end{aligned} \tag{5}$$

of Schleicher et al. (1993) one can immediately express the elements A and B of the 2×2 surface-to-surface ray propagator matrix in terms of β, K_{NIP}, K_N, and K_S. Using symmetry properties of the propagator matrix for a normal ray, the two other elements of the propgator matrix C and D can be expressed by A and B ($C = A^2/B - 1/B$ and $D = A$, see Schleicher et al. (1993)). Thus, the elements of the propagator matrix read

$$A = \frac{1}{K_{NIP} - K_N}\left(K_{NIP} + K_N - \frac{2\,K_S}{\cos\beta}\right) \tag{6a}$$

$$B = \frac{1}{K_{NIP} - K_N}\left(\frac{2v}{\cos^2\beta}\right) \tag{6b}$$

$$\begin{aligned} C = \frac{1}{K_{NIP} - K_N}\Bigg(&\frac{2\,K_{NIP}\,K_N\cos^2\beta}{v} \\ &-2(K_{NIP}+K_N)\frac{\cos\beta K_S}{v} + \frac{2K_S^2}{v}\Bigg) \end{aligned} \tag{6c}$$

$$D = \frac{1}{K_{NIP} - K_N}\left(K_{NIP} + K_N - \frac{2K_S}{\cos\beta}\right). \tag{6d}$$

The elements of the surface-to-surface ray propagator matrix are of use for a multitude of

$$
\begin{aligned}
t^2 = & \left[t_0 + \left(\frac{\sin\beta_G}{v_G} + \frac{\sin\beta_S}{v_S} \right) (x_m - x_0) + \left(\frac{\sin\beta_G}{v_G} - \frac{\sin\beta_S}{v_S} \right) (h - h_0) \right]^2 \\
& + 2\,t_0 \left[(x_m - x_0) \left(K_3 \frac{\cos^2\beta_G}{v_G} + K_2 \frac{\cos^2\beta_S}{v_S} \right) (h - h_0) \right. \\
& + \frac{1}{2} (x_m - x_0) \left((4\,K_1 - 3\,K_3) \frac{\cos^2\beta_G}{v_G} - K_2 \frac{\cos^2\beta_S}{v_S} \right) (x_m - x_0) \\
& \left. + \frac{1}{2} (h - h_0) \left(K_3 \frac{\cos^2\beta_G}{v_G} - K_2 \frac{\cos^2\beta_S}{v_S} \right) (h - h_0) \right] .
\end{aligned}
\tag{7}
$$

seismic applications, like the calculation of the geometrical spreading factor which plays an important role in true amplitude migration, or the determination of the Fresnel zone. These application are explained in detail by Schleicher et al. (2001).

Finite-offset CRS Stack

For the FO CRS Stack we use the five-parameter formula (7) as stacking operator which has been derived by means of paraxial ray theory (Zhang et al., 2001). The two linear parameters are the incidence angle β_S at the source S and the emergence angle β_G at the receiver G of the central ray. Source and receiver of the central ray have a finite half-offset h_0 and the midpoint coordinate x_0. They are located on a straight measurement line. The quadratic parameters are given by K_1, K_2, and K_3. K_1 is the wavefront curvature at G of a common-shot wave which originates in a point source at S and propagates along the central ray to G. K_2 and K_3 are the wavefront curvatures of a fictitious wave at S and G, respectively, for which each paraxial ray that starts at the point $x_0 - h$ on the measurement line emerges after reflection at $x_0 + h$. The five wavefield attribute β_S, β_G, K_1, K_2, and K_3 can be evaluated from the stacking parameters determined in the FO CRS Stack if the near-surface velocities v_S and v_G at S and G, respectively, are available.

One important feature of the FO CRS Stack is the ability to handle wave-type converted reflections as there could be any type of wave traveling along the central ray. For example, for a primary reflected wave with a P-S conversion on the reflector, v_S has to be set to the wave propagation velocity of P-waves and v_G to the wave propagation velocity of S-waves.

In Figure 2, we show a synthetic data example where the angles β_S and β_G determined with the FO CRS method for primary reflection with half-offset $h = 0.5$ km are compared to the forward-calculated values computed by ray-tracing. The four figures from the top to the bottom are associated with the primary reflections from the four interfaces of the model (Figure 3) in the same sequence. One can observe that the fully automatic extraction of the angles yields a good agreement with the forward calculated values. Both angles are important attributes and find their application, e.g., in Stereotomography (Billette and Lambaré, 1998). Further attributes and their application will be discussed in the oral presentation.

Conclusions

We have introduced a new analytic moveout formula for a curved measurement surface which may find application in a variety of seismic problems. Futhermore, we presented a traveltime formula with which one can simulate any specified FO section. Both formulas are independent of the laterally inhomogeneous velocity model. Only the near-surface velocity is required to extract wavefield attributes from the stacking parameters.

References

Billette, F., and Lambaré, G., 1998, Velocity macromodel estimation from seismic reflection data by stereotomography: Geophys. J. Int., **135**, 671–690.

Hubral, P., 1983, Computing true amplitude reflections in a laterally inhomogeneous earth: Geophysics, **48**, no. 8, 1051–1062.

Jäger, R., Mann, J., Höcht, G., and Hubral, P., 2001, Common-reflection-surface stack: Image and attributes: Geophysics, **66**, no. 1, 97–109.

Mann, J., Jäger, R., Müller, T., Höcht, G., and Hubral, P., 1999, Common-reflection-surface

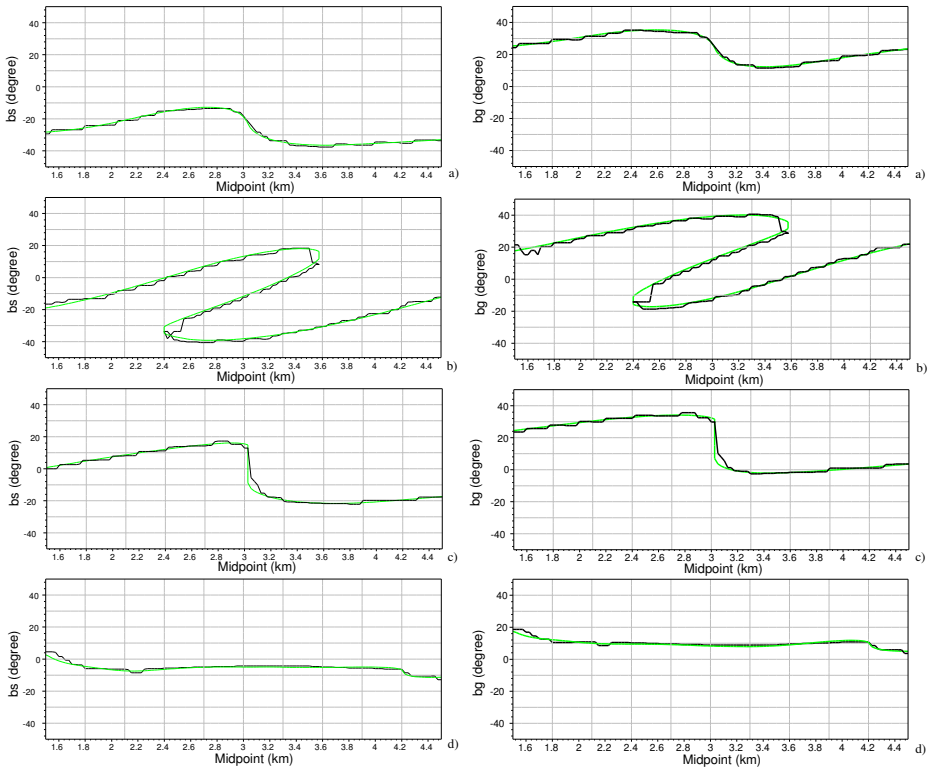

Figure 2: Attribute sections for the angles β_S (left) and β_G (right) in dependence of the midpoint for reflection with $h = 0.5$ km. The wiggly curves are data-derived, the smooth curves are forward-calculated.

stack - a real data example: J. Appl. Geoph., **42**, no. 3,4, 301–318.

Müller, T., Jäger, R., and Höcht, G., 1998, Common reflection surface stacking method - imaging with an unknown velocity model: 68th Annual Internat. Mtg., Soc. Expl. Geophys., Expanded Abstracts, 1764–1767.

Schleicher, J., Tygel, M., and Hubral, P., 1993, Parabolic and hyperbolic paraxial two-point traveltimes in 3D media: Geophys. Prosp., **41**, no. 4, 495–514.

Schleicher, J., Tygel, M., and Hubral, P., 2001, Seismic True Amplitude Reflection Imaging: To be published as SEG Monograph.

Zhang, Y., Bergler, S., Tygel, M., and Hubral, P., 2001, Model-independent traveltime attributes for 2-D, finite-offset multi-coverage reflections: Accepted by Pure Appl. Geophys.

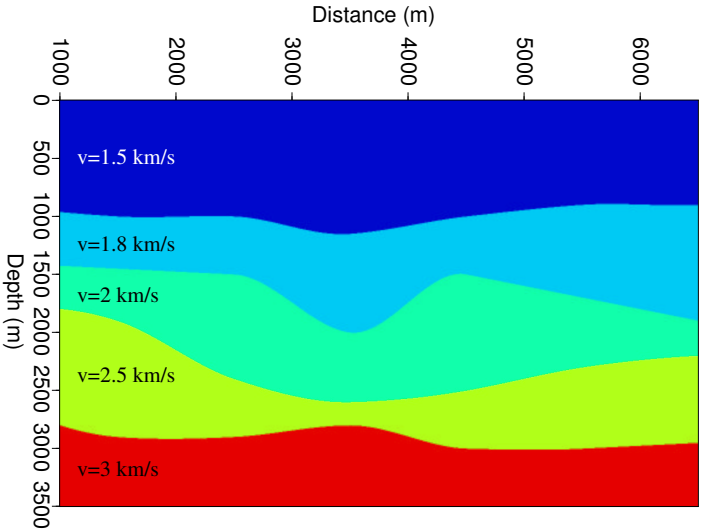

Figure 3: Model.

The role of interface waves and diffracted waves in the amplitude scattering phenomenon

Nathalie Favretto-Cristini[1] and Eric de Bazelaire[2]
[1] Centre National de la Recherche Scientifique-UMR5831 Imagerie Géophysique, Univ. Pau, BP 1155, 64013 Pau Cx, France.
[2] Total Fina Elf / Elf Exploration Production, CSTJF, Av. Larribau, 64018 Pau Cx, France.

Summary

Amplitude scattering, caused by the occurrence of thin gaps between layers, is a fractal phenomenon that may generate visible events on seismic sections, correlated from trace to trace but different from usual reflections, although of equivalent energy. The occurrence of these events, wrongly assumed as reflections, may lead to erroneous interpretation of real data, in particular when locating reflectors and inverting the amplitudes of reflected events. We argue that the near-field wave propagation in the vicinity of the geological contacts, and specially interface wave propagation and diffracted waves, is widely involved in the occurrence of the amplitude scattering phenomenon. Theoretical and phenomenological studies, performed at the present time, appear consistent with our assumptions.

Introduction

Interface scattering is a kind of scattering associated with a spatial distribution of irregular geological contacts at interfaces between layers. It has been previously shown that interface scattering is generally weak [1]. Only a few percent of incident energy are scattered and the scattered energy-to-transmitted energy ratio is about few percent. On the other hand, backscattered energy has the same order of magnitude as reflected energy that is composed of a few percent of incident energy. Consequently, it seems natural that in seismic-reflection, scattering phenomenon may occur on stacked sections and that neglecting this phenomenon may lead to significant errors. Interface scattering may affect the phase (phase scattering caused by interface roughnesses) and/or amplitude (amplitude scattering) of the incident wavefront. The effect of a phase scatterer, for example the weathered zone in land seismics, on reflected and transmitted signals has been investigated in a previous paper [1]. We discuss here about the amplitude scattering phenomenon, generally caused by the changes in the contact quality at interfaces between layers of the stratified earthground, resulting from erosion and/or tectonics processes.

The amplitude scattering phenomenon

In some particular cases of geological contacts (thin gaps between layers) and under certain conditions, amplitude scattering, that generally appears as a source noise, may generate on seismic sections some peculiar events, correlated from trace to trace, but different from usual reflections, although of equivalent energy. These events have low frequency spectra and their amplitude, different from the counterpart of usual reflections, depends greatly on the gap filling. Amplitudes greater than the reflection ones testify to the occurrence of gas in gaps [2], while weaker amplitudes, associated with P-S wave conversions, indicate the occurrence of gaps filled up with fluid (Fig.1). At the moment we do not have a full explanation for this observation.

In a previous paper [2], we have shown that finite-difference elastic (or poroviscoelastic) modeling of real events, using information as sonic and density logs recorded in wells, does not correctly simulate the real data amplitude in such particular geological contexts. Considering implicitly that the layers of stratified medium are in welded contact for simulating seismic events leads to neglect some additionnal phenomena which may take place in the vicinity of interfaces. We argue that dense distribution of gaps at interfaces, whose fractality has been clearly observed in situ [3], may affect some near-field wave phenomena, such as elastic wave reflection and interface wave propagation, that are generally assumed to be ineffective on the far-field wave propagation, detected by receivers in seismic-reflection. However, energy carried away by particular propagative diffracted waves or evanescent waves, such as interface waves or some diffracted waves, is, of course, not distributed to the other waves and specially to the reflected waves. As a consequence, neglecting such phenomena, that are no longer second-order phenomena in the problem of interest here, may lead to an incorrect energy balance, leading to an inaccurate local estimation of the amplitudes of seismic reflections. The main objective of our work is then to attempt to describe the physical mechanism and energy balance of the wave propagation in a complex layered medium with

lateral inhomogeneities at interfaces, so as to identify seismic events associated to reflection and amplitude scattering. What is important to know is therefore what happens in the vicinity of interfaces.

Are interface and diffracted waves guilty?

Some of the key problems encountered in the modeling of the amplitude scattering effects are the difficulty in considering the distribution of thin gaps in numerical schemes, and also the difficulty in describing its effect on the wave propagation in the vicinity of the interface between layers.

Considering the size of microcavities between layers and the characteristics of the seismic waves, it is not expected the diffraction effects to play an important part in the phenomenon of interest here. It is then considered that an effective theory based on homogeneization would be surely efficient enough for modeling wave propagation. However, results thus obtained are not satisfactory [1], as the fractality of the amplitude scattering phenomenon is assumed, and as interface wave propagation and diffraction effects of waves in the vicinity of gaps are no more second-order phenomena.

Fractality contains periodicity for all scales, and then for the measurement scale. By analogy with studies in Non Destructive Testing area or in Acoustics, the distribution of welded contact zones and gaps between layers of the stratified earthground can then act as a comb transducer [4]. The comb transducer is commonly used for excitation and detection of surface waves (Fig. 2). An incident P-wave, generated by an ultrasonic transducer, strikes the interface between the solid comb and the solid material, and is transformed into a surface wave (SW) at the end of the comb. The SW excitation is efficient since the incident wavelength is more or less equal to the spatial counterpart of the gap distribution. The SW, that propagates at the free solid surface, is then coherently recombined by the comb into a P-wave, that can be detected by another ultrasonic transducer. The incident wavelength then determines the size of the active gap distribution and this property is fractal. Moreover, due to the occurrence of the gap distribution between layers, the interface wave would probably radiate during its propagation due to diffraction effects at the gap tips.

Consider now the reflection and refraction of waves at an interface of two materials. Three important cases are to be under consideration. If $\Lambda >> \lambda_{inc}$ (Λ being the spatial wavelength of gap distribution and λ_{inc} the incident wavelength), diffracted waves in both media can be propagative or evanescent. If $\Lambda = 1/2\ \lambda_{inc}$, Bragg phenomena are involved. $\Lambda << \lambda_{inc}$ is the usual assumption of most of theories. Diffracted waves in both media are usually evanescent, and consequently they are neglected in models. However, for a specific set of medium properties and under certain conditions, the reflection of a P-wave can produce propagative diffracted waves whose direction is quite similar to that of incident wave (Fig. 3).

By analogy with the results presented above, we believe that scattering at interfaces is thus created if there are constructive interactions between the size of the fractal gap distribution and the characteristics of the exciting P-wave. Anyway, S-wave propagation can be stopped by gap zones whose thickness has the same order of magnitude as the particle displacement amplitude. Energy balance, and then local estimation of the amplitudes of seismic reflections, may be incorrect if interface wave and diffracted wave propagation is not taken into account in modeling in those particular geological contexts.

Conclusion

In some particular geological contexts (thin gaps between layers), and under certain conditions, may occur on seismic sections some peculiar events with amplitudes stronger or weaker than expected, associated to amplitude scattering, but wrongly assumed as reflections. By analogy with studies in Non Destructive Testing area or in Acoustics, we argued that the near-field wave propagation in the vicinity of the geological contacts, and specially interface wave propagation and diffracted waves, is widely involved in the occurrence of the amplitude scattering phenomenon. Consequently, interpretation of real data and local estimation of the amplitudes of seismic reflections may be inaccurate, if these wave phenomena, usually neglected but that are no longer second-order phenomena in the problem of interest here, are not taken into account.

At the present time, we analyze the near-field wave propagation by using the BIS method [5]. This method is efficient for the description of interface wave generation and propagation and wave scattering. Results thus obtained are very promising and appear consistent with our assumptions. In support of theory, experimental studies are also being carried out in laboratory conditions.

References

[1] de Bazelaire, E. and Favretto-Cristini, N. *Amplitude bias caused by interface scattering. Part I:*

Phase scattering. Part II: Amplitude scattering. Submitted to Geophysical Prospecting.
[2] Favretto-Cristini, N. and de Bazelaire, E. (2001) *Amplitude scattering phenomenon: is interface wave propagation guilty?* Expanded Abstract of the EAGE/SEG Research Workshop on Reservoir Rocks, Pau (France), 30 April-3 May. To be appeared.
[3] Blanco, J. Personal communication.
[4] Biryukov, S.V. *et al.* (1995) *Surface acoustic waves in inhomogeneous media*. Springer-Verlag.
[5] Danicki, E. (1999) Resonant phenomena in bulk wave scattering by in-plane cracks. J. Acoust. Soc. Am. 105(1),84-92.

Acknowlegement

Jacques Blanco (Total Fina Elf) is gratefully aknowledged for providing us Figure 1.

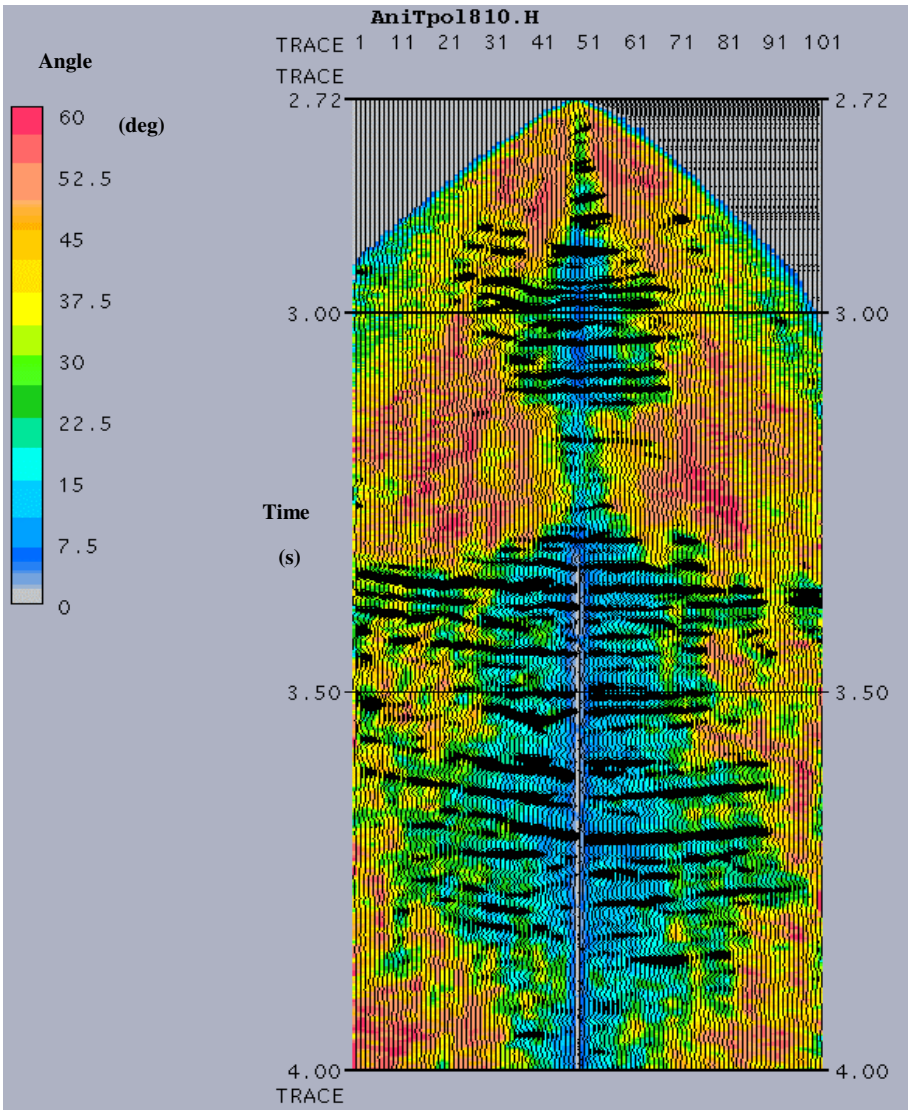

Fig.1. Wave arrivals observed on a walkaway imaging at polarization angles of 0 to 60 degrees with respect to vertical well. Only P-wave energy is represented. P-S wave conversions, noted here essentially in two zones (in red), are associated with very weak amplitudes of reflected waves. These anormalous amplitudes are to be compared with those of P-waves transmitted through the peculiar zones (water-saturated zones) with traveltimes around 3.00 and 3.50 seconds. From [3].

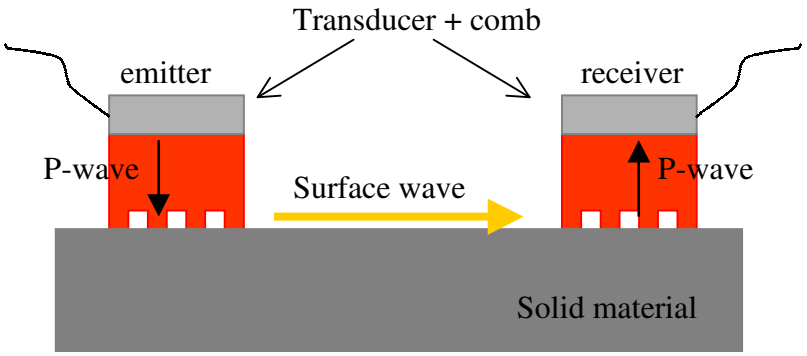

Fig.2. Generation and detection of surface waves by comb transducer in NDT area and in Acoustics.

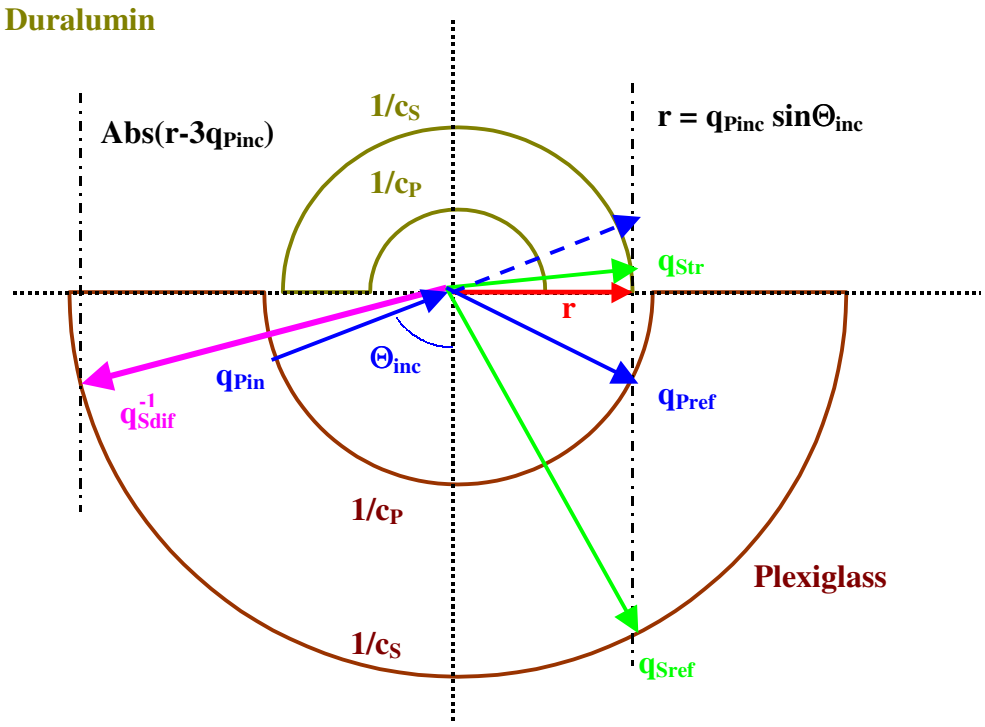

Fig.3. Slowness diagram illustrating wave diffraction (of order 0 and –1) at the Plexiglass/Duralumin interface for the case K=3 k_{inc}, K being the spatial wavenumber of the gap distribution and k_{inc} the incident P-wavenumber. **q** is the slowness vector defined by 1/c, c being the wave velocity in media. Only propagative waves are represented. The characteristics of media are assumed to be: c_P=2670m/s and c_S=1120m/s (Plexiglass), c_P=6440m/s and c_S=3170m/s (Duralumin). $\mathbf{q}_{Sdiff}^{-1}$ is the slowness vector associated to a S-diffracted (order –1) wave.

Towards Accurate Amplitudes for One-way Wavefield Extrapolation of 3-D Common Shot Records

Yu Zhang, James Sun, Samuel H. Gray, Carl Notfors, Veritas DGC Inc., and Norman Bleistein, Colorado School of Mines

Summary

We analyze the amplitudes produced by shot-record migration by one-way wavefield extrapolation. By comparing these amplitudes with those produced by true-amplitude Kirchhoff migration, we show the amplitude and phase errors that come from a standard implementation of migration by one-way wavefield extrapolation. Next, we present a new formulaton of shot-record migration that maintains its high fidelity in imaging complex structures, has correct dynamic behavior at least for constant velocity, and can be easily extended to $v(z)$. This formulation requires that we modify, in a straightforward way, the wavefield that is being downward continued. Our analysis applies equally to all migration methods based on one-way wavefield extrapolators.

Introduction

Until recently, Kirchhoff migration has been used for most 3-D prestack migrations, primarily because of its versatility and efficiency. The demands of imaging increasingly complex geological structures, however, have spurred a demand for increased imaging fidelity. This has led to the growing popularity of imaging methods that handle more than the single arrival (e.g., maximum-energy) that Kirchhoff migration is capable of handling conveniently. Such methods include multi-arrival Kirchhoff migration, which allows for several arrivals at each image location, and finite-difference migration, which allows for an unlimited number of arrivals at each image location. In this paper, we concentrate on one-way wavefield extrapolation, paying particular attention to its amplitude and phase behavior.

The standard formulation of finite-difference migration (Claerbout, 1985) consists of two parts. The first part is the downward continuation of the wavefields from the source and receiver locations using a "wave equation" that splits the wavefields into downgoing and upgoing parts. The second part is the application of an imaging condition, namely the division of the downward continued receiver wavefield by the downward continued source wavefield at each image point. Unfortunately, the one-way "wave equations" used in the downward continuation are not equivalent to the acoustic wave equation whose behavior they are designed to mimic. This lack of equivalence leads to a migrated wavefield that lacks correct amplitude and phase behavior, even though it is kinematically correct. By expressing the downward continued wavefields asymptotically, we are able to compare the imaged wavefield with the reflection coefficient of true amplitude Kirchhoff migration. The latter is our benchmark for amplitude and phase. The former is the downward continued receiver wavefield divided by the downward continued source wavefield. This comparison leads to a corrected equation for the upgoing and downgoing wavefields which, in turn, leads to a corrected expression for the wavefields being downward continued. When these corrections are applied, the migration produces images whose amplitudes and phases agree with true-amplitude Kirchhoff migration. These corrections are essentially without cost, and they do not compromise the migration's structural imaging fidelity, such as finite-difference migration.

Theory

We begin with a layered velocity ($v(z)$) earth and 3D common-shot migration. Given an acoustic wave-field p with source excitation at $\vec{x_s} = (x_s, y_s, 0)$ and $t = 0$,

$$\left(\frac{1}{v^2}\frac{\partial^2}{\partial t^2} - \frac{\partial^2}{\partial z^2} - \Delta\right) p(x, y, z; t) = \delta(\vec{x} - \vec{x_s})\delta(t), \quad (1)$$

(where $\Delta = \frac{\partial^2}{\partial x^2} + \frac{\partial^2}{\partial y^2}$), we record the surface data Q:

$$p(x_r, y_r, z = 0; t) = Q(x_r, y_r; t). \quad (2)$$

According to Bleistein et al.'s (2001) work on inversion, the true-amplitude common shot Kirchhoff inversion formula is (Zhang et al., 2000)

$$R(x, y, z) \sim \iiint i\omega \frac{\sqrt{\cos\alpha_{s0}\cos\alpha_{r0}}}{v_0}\sqrt{\frac{\psi_s\sigma_s}{\psi_r\sigma_r}} \; e^{i\omega(\tau_s+\tau_r)}\hat{Q}(x_r, y_r; \omega)dx_r dy_r d\omega, \quad (3)$$

where ψ and σ are in-plane and out-of-plane geometrical spreading terms and α_{s0} and α_{r0} are surface angles at

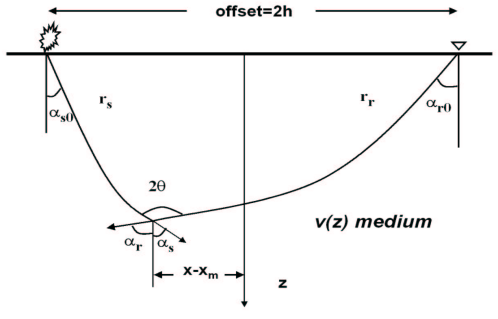

Fig. 1: Ray paths in a $v(z)$ medium.

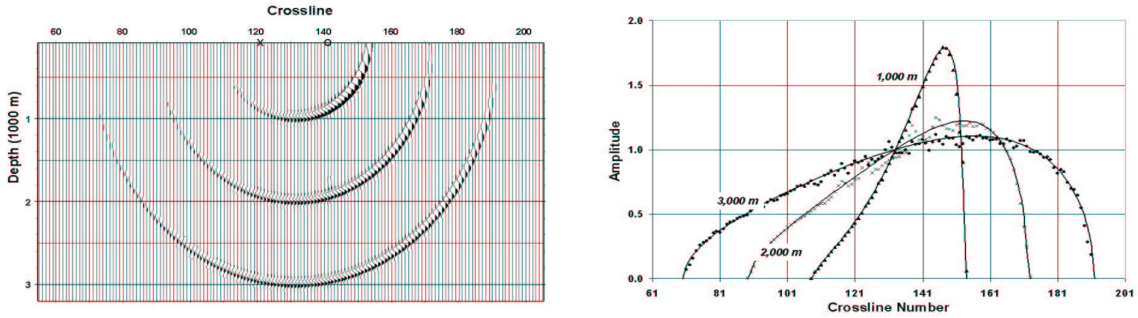

Fig. 2: Left: 3-D phase-shift migrated impulse responses along the center inline. The shot is at crossline 121 and receiver at crossline 141. Right: Amplitudes of the 3-D migrated impulse responses. The solid lines are theoretical predictions and symbols are the peak amplitudes from the left.

shot and receivers, respectively (see Figure 1), and the hat denotes temporal Fourier transform.

For conventional common-shot migration, we downward continue both shot and receiver wavefields:

$$\begin{cases} \left(\frac{\partial}{\partial z}+\Lambda\right) D = 0, \\ D(x,y,z=0;t) = \delta(\vec{x}-\vec{x_s})\delta(t), \end{cases} \tag{4}$$

and

$$\begin{cases} \left(\frac{\partial}{\partial z}-\Lambda\right) U = 0, \\ U(x,y,z=0;t) = Q(x,y;t) \end{cases} \tag{5}$$

where D and U are the downgoing and upgoing waves (Claerbout, 1985), respectively, and

$$\Lambda = \frac{1}{v}\frac{\partial}{\partial t}\sqrt{1-\left(\frac{\partial^2}{\partial x^2}+\frac{\partial^2}{\partial y^2}\right)\left(\frac{1}{v^2}\frac{\partial^2}{\partial t^2}\right)^{-1}}$$

is the square-root operator. To produce the image, we use the imaging condition

$$R(x,y,z) = \int \frac{\hat{U}(x,y,z;\omega)}{\hat{D}(x,y,z;\omega)}d\omega. \tag{6}$$

For a $v(z)$ medium, Zhang et al. (2001) give an asymptotic expression for the one-way wave fields:

$$\hat{D}(x,y,z;\omega) \sim \frac{i\omega}{2\pi}e^{-i\omega\tau_s}\sqrt{\frac{\cos\alpha_s}{\psi_s\sigma_s}} \tag{7}$$

and

$$\hat{U}(x,y,z;\omega) \sim \iint \frac{i\omega}{2\pi}\sqrt{\frac{\cos\alpha_r}{\psi_r\sigma_r}}e^{i\omega\tau_r}\hat{Q}dx_r dy_r. \tag{8}$$

Substituting (7) and (8) into (6), we obtain

$$R(x,y,z) \sim \iiint \sqrt{\frac{\cos\alpha_r\psi_s\sigma_s}{\cos\alpha_s\psi_r\sigma_r}}e^{i\omega(\tau_r+\tau_s)}\hat{Q}dx_r dy_r d\omega. \tag{9}$$

Comparing (9) with (3), we conclude that the algorithm (4-6) cannot provide the true amplitude image; even the phase term $i\omega$ is missing.

To see why this happens, we observe that for constant velocity, D and U are not components of the full wave fields p, but rather they are related to p by (Zhang, 1993)

$$D = \frac{1}{2}\left(\Lambda - \frac{\partial}{\partial z}\right)p,$$

$$U = \frac{1}{2}\left(\Lambda + \frac{\partial}{\partial z}\right)p,$$

and

$$D + U = \Lambda p.$$

Therefore from (1) and (2) we have

$$\begin{cases} \left(\frac{\partial}{\partial z}+\Lambda\right) D = \frac{1}{2}\delta(t)\delta(\vec{x}-\vec{x}_s), \\ \left(\frac{\partial}{\partial z}-\Lambda\right) U = \frac{1}{2}\delta(t)\delta(\vec{x}-\vec{x}_s), \\ (U+D)|_{z=0} = \Lambda Q(x,y;t), \end{cases} \tag{10}$$

Attaching physical meaning to D and U, we can reformulate (10) as follows:

$$\begin{cases} \left(\frac{\partial}{\partial z}+\Lambda\right) D = 0, \\ \left(\frac{\partial}{\partial z}-\Lambda\right) U = 0, \\ D|_{z=0} = \frac{1}{2}\delta(t)\delta(\vec{x}-\vec{x_s}), \\ U|_{z=0} = \Lambda Q(x,y;t). \end{cases} \tag{11}$$

Noting that the symbol of Λ in the Fourier domain is

$$\lambda = i\frac{\omega}{v}\sqrt{1-v^2\frac{k_x^2+k_y^2}{\omega^2}},$$

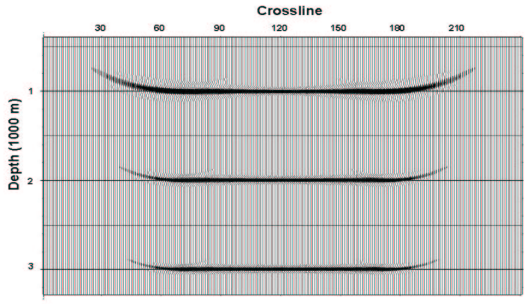

Fig. 3: Flat reflectors along the center inlines after 3-D common shot migration.

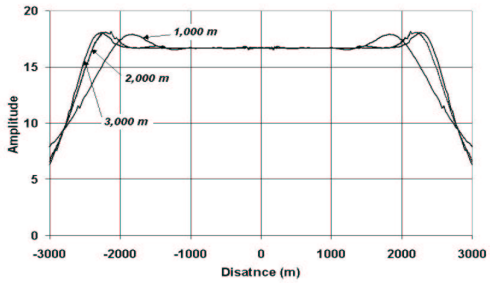

Fig. 4: Peak migrated amplitudes of the three reflectors in Figure 3.

we see that the modified initial condition for U gives an additional phase shift $i\omega$. We also need to modify the imaging condition to be

$$R(x,y,z) = \int \frac{\hat{p}_U(x,y,z;\omega)}{\hat{p}_D(x,y,z;\omega)} d\omega. \qquad (12)$$

Here p_D and p_U are defined as

$$p_D = \Lambda^{-1} D, \qquad p_U = \Lambda^{-1} U,$$

which satisfy $p_D + p_U = p$. It is easy to see p_U and p_D are downgoing and upgoing waves (p^+ and p^-) introduced in Wapenaar (1998). Noticing $\lambda = i\frac{\omega}{v}\cos\alpha$ and applying stationary phase to (11) and (12), we obtain

$$R(x,y,z) \sim \iiint \frac{\cos\alpha_{r0}}{v_0} \sqrt{\frac{\cos\alpha_s \psi_s \sigma_s}{\cos\alpha_r \psi_r \sigma_r}} \; e^{i\omega(\tau_r+\tau_s)} \hat{Q} dx_r dy_r d\omega. \qquad (13)$$

For constant velocity, the splitting (10) is exact. Therefore (11) and imaging condition (12) give the true-amplitude result. This can be directly seen by comparing (13) with (3) and setting $\alpha_{s0} = \alpha_s$, $\alpha_{r0} = \alpha_r$. For the $v(z)$ case, we need to apply another correction term

$$\sqrt{\frac{\cos\alpha_{s0}}{\cos\alpha_s}\frac{\cos\alpha_r}{\cos\alpha_{r0}}},$$

or

$$\sqrt{\frac{\lambda_{s0}}{\lambda_s}\frac{\lambda_r}{\lambda_{r0}}}.$$

Research is currently in progress on modifying the differential operators in (10) to include this factor in the resulting D and U.

Numerical results

Figure 2 (left) shows the 3-D migrated impulse responses along the center inline from a trace with three 7.5 Hz Ricker wavelets at depth 1000m, 2000m and 3000m, respectively. The source is at crossline 121 and receiver at crossline 141 and trace spacing is 50m in both inline and crossline directions. The medium velocity is 2000m/s. Unlike the kinematic behavior, the amplitudes of the impulse responses are asymmetric, with a bias on the receiver side. The peak amplitudes along the impulse responses are in good agreement with the theoretical prediction shown in Figure 2 (right).

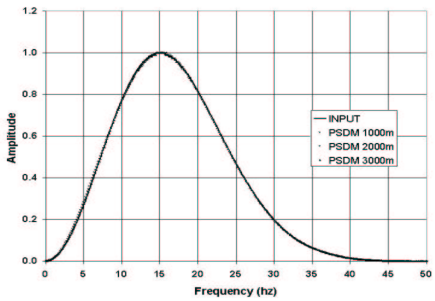

Fig. 5: Frequency spectrum of the migrated wavelets at inline 121 and crossline 121. The solid line is the spectrum of the input 15 Hz Ricker wavelet. The overlay is nearly perfect.

Figure 3 is the center inline of the 3-D migrated result from a single shot over three flat reflectors. The peak amplitudes along the three migrated reflectors are shown in Figure 4. Aside from the edge effects and small jitters caused by interference with wraparound artifacts, the 3-D common shot migration recovers the reflectivity accurately. Figure 5 shows that the frequency content is preserved by the migration at the center trace location. However, the wavelet becomes progressively lower frequency away from the center trace due to the effects of stretching and anti-aliasing.

The next example is from the 3-D SEG-EAGE salt model. The "area shot" dataset was selected over the marine streamer C3-NA dataset because of size considerations. However, this "area shot" dataset is known to produce

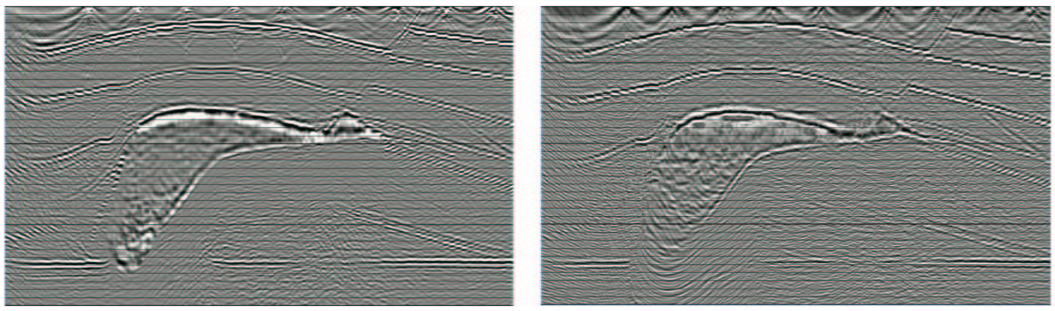

Fig. 6: Inline 242 of the SEG-EAGE model: migrated images from the optimized finite difference algorithm (left) and a single-arrival Kirchhoff migration algorithm (right).

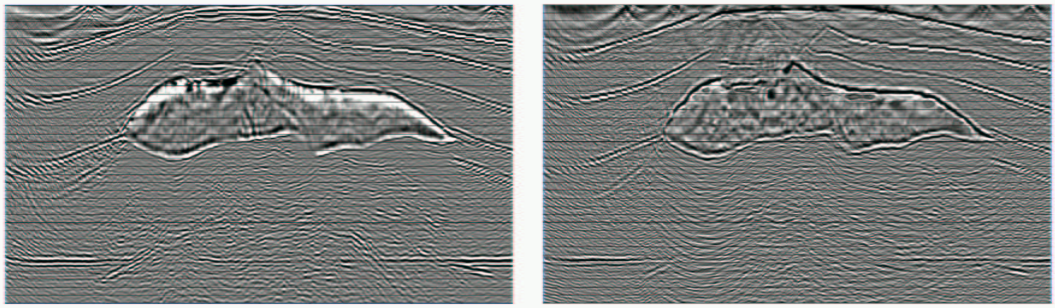

Fig. 7: Inline 342 of the SEG-EAGE model: migrated images from the optimized finite difference algorithm (left) and a single-arrival Kirchhoff migration algorithm (right).

relatively noisy results since it contains only 45 shots. The hybrid finite-difference (Sun et al., 2001) migrated results at inlines 242 and 342, compared with results from the "maximum energy" Kirchhoff migration, are shown in Figures 6 and 7. The finite-difference migrated images show much better imaged salt bottoms. The subsalt flat event images are also significantly improved. Moreover, the finite-difference images do not show the typical "ghost smiles" routinely observed in Kirchhoff-migrated images.

Conclusions

Migrations beased on one-way wavefield extrapolation offer the potential of greater structural imaging quality than single-arrival Kirchhoff migration, but the standard formulation of such migrations, e.g. finite-difference migration, produce incorrect migrated amplitudes. By comparing these amplitudes with those produced by true-amplitude Kirchhoff migration, we have, in effect, calibrated these migration methods, correcting their amplitude and phase behavior.

References

Bleistein, N., Cohen, J. K., and Stockwell, J. W., 2001, Mathematics of multidimensional seismic inversion: Springer.

Claerbout, J., 1985, Imaging the earth's interior: Blackwell Scientific Publications, Inc.

Sun, J., Notfors, C., Gray, S., and Zhang, Y., 2001, 3-D pre-stack common shot depth migration: a structure adaptive implementation: submitted to SEG 2001.

Wapenaar, K., 1998, Reciprocity properties of one-way propagators: Geophysics, **63**, no. 4, 1795–1798.

Zhang, Y., Gray, S., and Young, J., 2000, Exact and approximate weights for Kirchhoff migration: 70th Ann. Mtg., Soc. Expl. Geophys., Expanded Abstracts, **II**, 1036–1039.

Zhang, Y., Gray, S., and Young, J., 2001, True-amplitude common-offset, common-azimuth $v(z)$ migration: submitted to Journal of Seismic Exploration.

Zhang, G. Q., 1993, System of coupled equations for upgoing and down-going waves: Acta Math. Appl. Sinica, **16**, no. 2, 251–263.

Velocity analysis in the scattering-angle/azimuth domain

Sverre Brandsberg-Dahl[†], *Bjørn Ursin*[‡] *and Maarten V. de Hoop*[†]

Abstract

We present a method for migration velocity analysis in complex media that does not depend on picking traveltime misfits or residual moveout in common image gathers (CIGs). Our method constructs CIGs in the scattering-angle/azimuth domain, where we apply semblance or differential semblance to measure the coherency of events. Since amplitude versus angle (AVA) effects will degrade the performance of any semblance based velocity analysis, we perform an AVA compensation to the CIGs before applying the semblance measure. Any residual curvature or AVA effects in the resulting CIGs are then back projected to form an update of the background model.

The theory is developed for in-homogeneous anisotropic elastic media, and we show two short examples from isotropic elastic models.

Introduction

One of the core problems in seismic imaging and inversion is to estimate a correct background model. To create an image based on the assumption of a linearized scattering problem, a correct smooth background model is crucial when calculating the Green's functions needed in any imaging algorithm. In general the problem is the same regardless of assumptions about the media and experiment configuration; we need to find a smooth model that prescribes a wave propagation that is similar to the propagation the real data have experienced. The problem of estimating this background model has in general been cast as an optimization problem, where the goal is to minimize some misfit function with respect to the parameters in the background model. The optimization can be either global, trying to fit the model to the data in one complex operation, or local where only a small portion of the model is treated at a time (Cruz et al., 2000). Most of the methods in use in the industry today rely heavily on human interaction such as tideous picking of events and interpretation of curvatures in common image gathers. In areas with complex geology, accurate velocity analysis is performed through an iterative run of pre-stack depth migrations and picking/interpretation, something that can contribute a great portion of the total processing cost of a data set.

Here, we present a method that is based on local optimization, is more or less automatic, and does not require any picking of traveltimes. We use the generalized Radon transform (Beylkin and Burridge, 1990) to image the seismic data, a procedure which naturally introduces the image-point related coordinates: migration dip $\boldsymbol{\nu}$, scattering-angle θ, and azimuth ψ. With these parameters we are able to properly parametrize the problem in a single-valued fashion at the image point (De Hoop and Brandsberg-Dahl, 2000). To prepare the resulting angle domain common image gathers for velocity analysis, we perform a AVA compensation to remove amplitude variations along the events. The quality of the current background velocity model is assessed by analyzing the coherency in the angle CIGs, and the update is formed by a tomographic back projection of the image gather misfits.

Common image gathers in the angle domain

We consider wave propagation and scattering in a domain $\mathcal{D} \subset \mathbb{R}^3$ with non-intersecting acquisition surfaces $\partial S \times \partial R$. The Cartesian position vector in the configuration is $\boldsymbol{x}$ and the source and receiver positions, constrained to ∂S and ∂R, are $\boldsymbol{s}$ and $\boldsymbol{r}$. The medium is described by density ρ and the elastic stiffness tensor c_{ijkl}. We assume that the medium can be represented by a smooth background component, indicated by the superscript $^{(0)}$, and a rapidly varying perturbation, indicated by the superscript $^{(1)}$.

We produce common image gathers (CIGs) in the scattering-angle/azimuth domain by shooting the rays from the image point to the surface. This allows for a direct construction of angle domain CIGs by using the incomplete inverse generalized Radon transform (GRT) (Brandsberg-Dahl et al., 2000). The source and receiver positions are determined from where the rays intersect the acquisition surface and they are both functions of the angle coordinates at the image point, i.e. $\boldsymbol{s} = \boldsymbol{s}(\boldsymbol{x}, \boldsymbol{\nu}, \theta, \psi)$. The image gathers for scattering angle θ and azimuth

[†]Center for Wave Phenomena, Colorado School of Mines, Golden CO 80401, USA

[‡]Department of Petroleum Technology and Applied Geophysics, Norwegian University of Science and Technology, N-7491 Trondheim, Norway

$\psi_{\boldsymbol{x}}$ is

$$\mathcal{I}_k(\boldsymbol{x},\theta_{\boldsymbol{x}},\psi_{\boldsymbol{x}}) =$$

$$\frac{1}{\pi}\mathrm{Re}\int_0^\infty(-\mathrm{i}\omega)\mathrm{d}\omega\,\frac{1}{8\pi^2}\int_{E_{\boldsymbol{\nu}}(\theta,\psi)}\mathcal{B}_k(\boldsymbol{x},\boldsymbol{\nu}_{\boldsymbol{x}},\theta_{\boldsymbol{x}},\psi_{\boldsymbol{x}})$$

$$\cdot\,\widehat{\xi}_p(\boldsymbol{r})\,U^{(1)}_{pq}(\boldsymbol{r},\boldsymbol{s},\omega)\,\widetilde{\xi}_q(\boldsymbol{s})\,\exp[-\mathrm{i}\omega T_k(\boldsymbol{x})]\,\mathrm{d}\boldsymbol{\nu}_{\boldsymbol{x}}\,. \quad (1)$$

Here k is an index corresponding to the different reflection modes i.e. *PP* and *PS*, $\mathcal{B}_k$ is a properly weighted amplitude term, T_k is traveltime, $U^{(1)}_{pq}$ is the seismic data and $\widetilde{\xi}_q$ and $\widehat{\xi}_p$ are the polarization vectors at the source and receiver (ray end-points) respectively. The ray geometry and the related quantities in the unperturbed medium are shown in solid black in Figure 1.

The gradient of the image is taken with respect to the background medium parameters grouped together in the vector $\boldsymbol{m} = \{c^{(0)},\rho^{(0)}\}$, and corresponds to a Frechét derivative of equation (1). To get an explicit integral representation of the gradient we proceed by a direct differentiation

$$\frac{\partial\mathcal{I}_k}{\partial m_i}(\boldsymbol{x},\theta_{\boldsymbol{x}},\psi_{\boldsymbol{x}}) \simeq$$

$$\frac{1}{\pi}\mathrm{Re}\int_0^\infty(-\mathrm{i}\omega)\mathrm{d}\omega\,\frac{1}{8\pi^2}\int_{E_{\boldsymbol{\nu}}(\theta,\psi)}\mathcal{B}_k(\boldsymbol{x},\boldsymbol{\nu}_{\boldsymbol{x}},\theta_{\boldsymbol{x}},\psi_{\boldsymbol{x}})$$

$$\left\{\left\{\frac{\partial\widehat{\xi}_p(\boldsymbol{r})}{\partial m_i}\,U^{(1)}_{pq}\,\widetilde{\xi}_q(\boldsymbol{s}) + \widehat{\xi}_p(\boldsymbol{r})\,U^{(1)}_{pq}\,\frac{\partial\widetilde{\xi}_q(\boldsymbol{s})}{\partial m_i}\right\} +\right.$$

$$\left\{\widehat{\xi}_p(\boldsymbol{r})\left[\frac{\partial U^{(1)}_{pq}}{\partial\boldsymbol{r}}\frac{\partial\boldsymbol{r}}{\partial m_i} + \frac{\partial U^{(1)}_{pq}}{\partial\boldsymbol{s}}\frac{\partial\boldsymbol{s}}{\partial m_i}\right]\widetilde{\xi}_q(\boldsymbol{s})\right\} +$$

$$\left.\left\{\frac{\partial T_k(\boldsymbol{x})}{\partial m_i}(-\mathrm{i}\omega)\right\}\right\}$$

$$\widehat{\xi}_p(\boldsymbol{r})\,U^{(1)}_{pq}\,\widetilde{\xi}_q(\boldsymbol{s})\,\}\,\exp[-\mathrm{i}\omega T_k(\boldsymbol{x})]\,\mathrm{d}\boldsymbol{\nu}_{\boldsymbol{x}}\,. \quad (2)$$

The partial derivatives with respect to the medium are calculated by ray perturbation theory for fixed initial directions, as shown in Figure 1. Even though the initial ray directions are kept fixed, the initial slowness may change in order to satisfy the Eikonal equation in the initial point. As indicated in the figure, a typical outcome of perturbing the medium is a set of new rays that reaches the surface at different locations and with different slownesses. The data derivatives can be calculated using any standard numerical differentiation operator applied to the data. Note how the gradient contains weights both from the "image misfit" as well as from the "data change" at the surface. This is due to the novel parametrization of the velocity analysis, and ultimately leads to a tomographic back projection procedure that is carried out with data driven weight instead of the conventional picked traveltime misfit

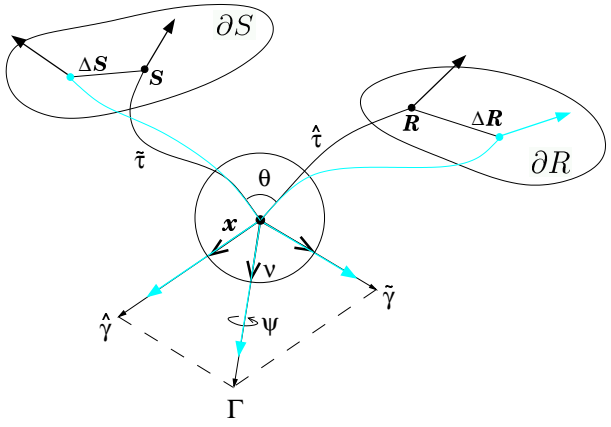

Figure 1: The ray geometry in both the reference and the perturbed medium. The perturbed ray quantities correspond to perturbing the medium while keeping the initial conditions fixed.

Semblance and differential semblance

To reveal the degree of coherency in the CIGs produced by applying equation (1) in the current background model $\boldsymbol{m}$, we introduce the following misfit functional

$$J[\boldsymbol{m}] = \frac{1}{2}\sum_k\int|\mathcal{L}\,\mathcal{I}_k(\boldsymbol{x},\theta_{\boldsymbol{x}},\psi_{\boldsymbol{x}})|^2\,\mathrm{d}\boldsymbol{x}\,\mathrm{d}\theta_{\boldsymbol{x}}\,\mathrm{d}\psi_{\boldsymbol{x}}\,, \quad (3)$$

where $\mathcal{L}$ is an operator that does not depend on $\boldsymbol{m}$. The integral is taken over "everything": all available image points, scattering-angles and azimuths, and the sum over k represent different modes of reflection i.e. *PP* and *PS*. To obtain the stack power functional we set

$$\mathcal{L} = \mathcal{L}_{SP} = 1\,, \quad (4)$$

and the optimal background is found by maximizing $J_{SP}[\boldsymbol{m}]$. The maximum is achieved when all the events in the CIGs sum constructively over the full range of angles. An obvious problem with this measure will be in a situation where the reconstructed perturbation changes sign due to an incomplete AVA compensation i.e. an incomplete

correction for polarity reversal in the reflection coefficient, and the full sum fails to be constructive. In such a situation we might have that the stack of an event in the CIG equals zero, even though the background model was correct in the sense that the event was perfectly flat.

The differential semblance functional is obtained by setting

$$\mathcal{L} = \mathcal{L}_{DS} = \partial_{(\theta,\psi)} = \frac{\partial^2}{\partial\theta\partial\psi}\,, \tag{5}$$

and the optimal background is found by minimizing $J_{DS}[\boldsymbol{m}]$. The derivative measures the similarity between adjacent traces in the CIGs. If the "neighboring inversions" (traces) in the CIGs are exact alike, the result of applying equation (3) is zero. That is, an event should appear at the same spatial location and have a uniform amplitude signature in the different reconstructions, independent of the scattering-angle and azimuth. The derivative $\partial_{\theta,\psi}$ measures the extent to which this is the case.

Since we will use a gradient based optimization scheme, we need to compute the gradient of equation (3) with respect to the medium parameters. Applying the chain rule and differentiating with respect to the medium $\boldsymbol{m}$ we get

$$\frac{\partial J[\boldsymbol{m}]}{\partial m_i} = \sum_k \int \mathcal{L}\,\mathcal{I}_k(\boldsymbol{x},\theta_{\boldsymbol{x}},\psi_{\boldsymbol{x}}) \cdot \mathcal{L}\,\frac{\partial \mathcal{I}_k(\boldsymbol{x},\theta_{\boldsymbol{x}},\psi_{\boldsymbol{x}})}{\partial m_i}\,\mathrm{d}\boldsymbol{x}\,\mathrm{d}\theta_{\boldsymbol{x}}\,\mathrm{d}\psi_{\boldsymbol{x}}\,. \tag{6}$$

The form of this gradient can be interpreted as a back projection of traveltime and polarization misfits through the term $\partial\mathcal{I}_k/\partial m_i$, weighted by the energy (misfit) in the CIGs $\mathcal{L}\mathcal{I}_k$ (see equation (2) and Figure 5).

Optimization scheme

Assuming that the misfit functional belongs to the class of multivariate smooth functions, we are free to choose an optimization scheme from a large variety of standard procedures. For simplicity, and based on experiences from earlier trails (Chauris and Noble, 1998), we will solve the optimization problem using a conjugate-gradient algorithm. At each iteration i, the conjugate-gradient method provides a search direction $\boldsymbol{p}_i$, along which we have to minimize the functional $J[\,\cdot\,]$. The minimization is performed as a line search for an optimal step-length α_i (positive scalar), such that $J[\boldsymbol{m}_i+\alpha_i\boldsymbol{p}_i]$ is minimized. The search direction in the conjugate-gradient scheme is constructed as a linear combination of the current gradient vector $\boldsymbol{g}_i = \nabla_{\boldsymbol{m}} J(\boldsymbol{x})$, calculated using equation (6), and the previous search direction. The medium update at the end of the current iteration is a step of length α_i in the direction $\boldsymbol{p}_i$: $\boldsymbol{m}_{i+1} = \boldsymbol{m}_i + \alpha\boldsymbol{p}_i$.

Results

We show two examples to illustrate the performance of our method. First a simple 1-D velocity model with three horizontal reflectors, with synthetic data generated by raytracing. The result of the velocity analysis is shown in Figures 2 and 3, Starting from a homogeneous initial model with $v = 1500$m/s, the method provides a satisfactory convergence in two iterations.

The second example is from the "Gas-cloud" model (Brandsberg-Dahl et al., 2000), where the data is generated by isotropic elastic finite-difference modeling. This model has a low velocity lens in the overburden of the otherwise simple ($v(z) = 1600 + 0.45z$) P-wave velocity profile, causing the P wavefield to fold and triplicate. A smoothed version of the true model is shown at the top of Figure 4. Figure 5 shows a CIG from the location marked by a black line in Figure 4 for five iterations during the optimization. At each step the CIG is shown with the corresponding component of the gradient to give an indication of where this particular CIG contribute in the model update. In iteration three, when most of the residual moveout is present at large scattering angles, the gradient clearly reflects the same behavior along the corresponding rays through the model. The final inverted velocity model is shown in the middle of Figure 4 and the difference between the true and inverted model is shown at the bottom.

Conclusions

We have presented a method that will allow us to perform velocity analysis in a highly automatic way. It eliminates the need for picking events in common image gathers or picking of traveltime misfits. The method presented here uses the misfit in the angle CIGs as weights in the tomographic updating of the background model, and provide us with a background model that minimizes the difference between adjacent traces in the CIGs. Before the lateral comparison we remove any angle-dependent variations in the reflectivity by undoing the effect of the point contrast-source radiation pattern, making the reconstructed quantity independent of any angular effects but errors in the background medium.

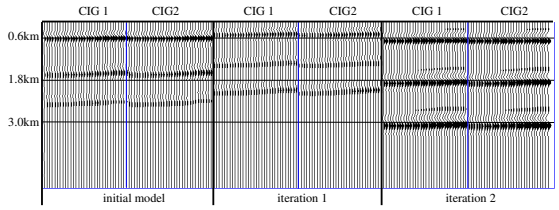

Figure 2: CIGs from the 1-D model with velocity profile $v(z) = 1600.0 + 0.4z$. The reflectors are at 0.6km, 1.8km and 3.0km. We use two CIGs during the velocity analysis with scattering angles ranging from 0^0 to 60^0. At the left are the CIGs in the initial velocity model, and a satisfactory flatness is achieved in only two iterations.

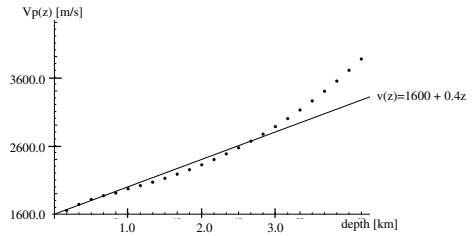

Figure 3: The velocity model (dots) obtained after the two iterations superimposed on the true $v(z)$ profile. The inverted model starts to deviate at depths beyond the deepest reflector in the data at 3.0km.

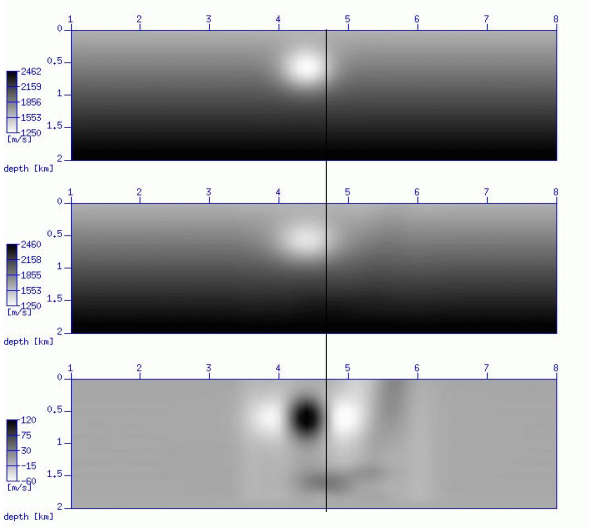

Figure 4: The true velocity model (top) and the inverted model obtained after six iterations (middle) and the difference.

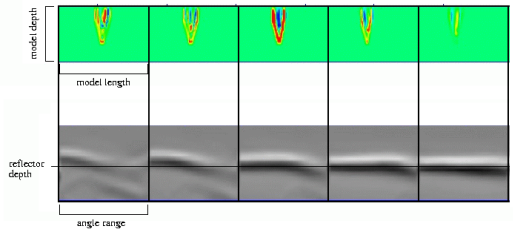

Figure 5: A sequence of gradients from the Gascloud model (top of figure). The gradients represent the same CIG, but for various stages of the model update. The corresponding CIGs are shown in the bottom half of the figure. The model is improved (updated) moving right in the figure, resulting in better focused CIGs and reduced values in the gradient.

Acknowledgments

Sverre Brandsberg-Dahl wants to thank BP Upstream Technology Group for hosting him during the completion of this work. He also thanks BP Norway and The Norwegian Research Council for financial support.

References

Beylkin, G., and Burridge, R., 1990, Linearized inverse scattering problems in acoustics and elasticity: Wave Motion, **12**, 15–52.

Brandsberg-Dahl, S., De Hoop, M., and Ursin, B., 2000, Focusing in dip and ava compensation on scattering-angle/azimuth gathers: submitted to Geophysics.

Chauris, H., and Noble, M., 1998, Testing the behavior of differential semblance for velocity estimation: 68th Ann. Internat. Mtg., Expanded Abstracts.

Cruz, J. C. R., Hubral, P., Tygel, M., Schleicher, J., and Höcht, G., 2000, The common reflecting element (CRE) method revisited: Geophysics, **65**, no. 3, 979–993.

De Hoop, M. V., and Brandsberg-Dahl, S., 2000, Maslov extension of generalized radon transform inversion in anisotropic elastic media:a least-squares approach: Inverse Problems, **16**, 519–562.